IUST
Iran University of Science and Technology

Iranian Journal of Electrical and Electronic Engineering

Journal Homepage: ijeee.iust.ac.ir

Open EMS Based Design of a CSRR Bandpass Filter for 5G: An Accessible Simulation Approach

Gauravkumar Asari*(C.A.)

Abstract: Bandpass filters (BPFs) are critical components in 5G radio-frequency front-end systems, where wide bandwidth, low insertion loss, and compact size are simultaneously required. In this paper, a metamaterial-inspired wideband BPF based on Complementary Split Ring Resonators (CSRRs) loaded with a dumbbell-shaped Defected Ground Structure (DGS) is proposed for mid-band 5G applications centered at 4.7 GHz. Unlike conventional designs that rely on commercial electromagnetic solvers, the proposed filter is developed and analyzed using a fully open-source electromagnetic simulation framework based on Open EMS, enabling cost-effectiveness and design reproducibility. The design evolution from a single-ring CSRR to a triple-ring configuration is systematically presented to enhance magnetic coupling and bandwidth. The incorporation of a dumbbell-shaped DGS further modifies the ground current distribution, leading to improved selectivity and reduced insertion loss. The optimized filter achieves a fractional bandwidth of approximately 43%, a minimum insertion loss of 0.72 dB, and a return loss better than -35 dB using a low-cost FR-4 substrate. Comprehensive parametric analysis, metamaterial characterization, group delay response, and electromagnetic field distribution are provided to validate the proposed approach. The results demonstrate that the open-source Open EMS-based methodology can achieve performance comparable to commercial solvers, offering an accessible and reliable design pathway for next-generation microwave filter development.

Keywords: Bandpass Filter, Complementary Split Ring Resonator, Defected Ground Structure, Scattering Parameters, Open EMS.

1 Introduction

THE advent of 5G communication systems has ushered in a new era of wireless connectivity that demands high speed data transmission, low latency, and efficient spectrum utilization. To support these requirements, especially in the mid-band frequency range (3 to 6 GHz), it is crucial to design compact and high-performance RF front-end components, with BPFs playing a central role in suppressing unwanted signals and defining operational bandwidth [1].

Conventional filter designs, based on lumped elements [2], [3],[4], cavity resonators [5], [6][7], SAW/BAW [8],[9], plasmonics [10], [11], [12] and planar microstrip line [13], [14] , often face limitations in terms of size, bandwidth, and selectivity, especially when scaled for 5G applications. Recent developments in metamaterials have opened new avenues in filter engineering by enabling materials and structures with engineered electromagnetic responses not found in nature. CSRRs have demonstrated great promise in achieving miniaturization, negative refractive index, and reconfigurable passband characteristics [15], [16], [17].

Over the past two decades, substantial research has been directed toward developing metamaterial-inspired BPFs leveraging CSRRs and DGSs to achieve compact

Iranian Journal of Electrical & Electronic Engineering, 2026.
Paper first received 28 Nov 2025 and accepted 05 Feb 2026.
* The author is with the Department of Electronics and Communication Engineering, Vishwakarma Government Engineering College, Chandkheda-382424, Ahmedabad, Gujarat, India
Corresponding Author: Gauravkumar Asari.
E-mail: grasari@vgceg.ac.in

size, high selectivity, and tailored frequency responses. Foundational studies on composite right/left-handed (CRLH) and CSRR structures have established the theoretical basis for achieving negative permittivity and permeability in planar devices, forming the cornerstone of left-handed filter design [18]. Several works have demonstrated dual-wideband performance by embedding CSRRs in substrate-integrated waveguide (SIW) platforms [19], while others have incorporated periodic CSRR cells as DGSs within half-mode SIWs (HMSIWs) to enhance compactness and stopband suppression [20]. Novel geometries such as hexagonal complementary cells have also been explored in SIW/HMSIW structures for tunability [21], though these approaches remain waveguide centric. Microstrip implementations, including those using open CSRRs, have shown potential for wider passbands [22], yet most report relatively modest bandwidths and do not systematically analyze multi-ring CSRR arrangements. Investigations into multilayer stripline CSRR coupling have provided valuable insight into field interactions and miniaturization [23], but their multilayer nature increases fabrication cost. Left-handed BPF demonstrations on premium laminates have confirmed negative-index operation with good selectivity [24], though substrate cost remains a barrier for mass adoption. Multi-split SRR geometries have been shown to realize double-negative behavior across multiple bands [25], and modified CSRR-DGS configurations have delivered sharper cut-offs and extended stopbands [26], [27], [28] albeit often prioritizing stopband purity over mid-5G passband performance.

Numerous studies have reported narrowband, wideband, and multiband BPFs employing CSRRs in microstrip and SIW platforms, often combined with DGS to enhance selectivity and bandwidth. While these approaches demonstrate promising performance, most reported designs rely on commercial electromagnetic solvers and expensive substrates, which limit reproducibility and accessibility for academic and low-cost research environments. Furthermore, detailed discussions on open-source simulation workflows and systematic design evolution of CSRR-based filters remain limited in existing literature.

In this work, an open-source electromagnetic simulation-based design methodology is proposed for the development of a wideband CSRR-based BPF using Open EMS, an open-source finite-difference time-domain (FDTD) electromagnetic solver. The proposed filter integrates a dumbbell-shaped DGS with a progressively evolved CSRR configuration to enhance bandwidth and reduce insertion loss. By adopting a low-cost FR-4 substrate and a fully reproducible simulation workflow, the presented approach bridges the gap between high-performance filter design and accessibility. The proposed design is systematically analyzed through parametric studies, metamaterial characterization using the Nicolson Ross Weir (NRW) method, group delay evaluation, and electromagnetic field distribution, demonstrating its suitability for mid-band 5G applications.

2 Design Methodology

The objective of this work is to design and optimize a compact BPF that operates efficiently in the mid-band 5G frequency range centered at 4.7 GHz, using metamaterial-inspired techniques. The filter utilizes CSRRs and DGS to enhance performance in terms of insertion loss, return loss, bandwidth, and compactness.

2.1 Substrate and Frequency Specifications

All layouts are designed on a low-cost FR-4 substrate, which is widely available and compatible with standard PCB fabrication processes. The material properties used are indicated in Table 1.

Table 1. Specifications of the Substrate for the Proposed BPF

Parameter	Value
Substrate Type	FR-4
Relative Permittivity (ε_r)	4.4
Thickness (h)	1.6 mm
Loss Tangent (tan δ)	0.02
Center Frequency (f_0)	4.7 GHz

2.2 Design Concept and Filter Structure

The BPF design evolves across three layouts (L_1, L_2, L_3), each progressively incorporating more complex geometries to enhance performance.

The design of the proposed BPF is initiated through a systematic evolution of the CSRR geometry. Initially, a single-ring CSRR etched on the ground plane is considered, as it represents the simplest complementary metamaterial unit capable of introducing a resonant stopband in planar transmission lines. This configuration is selected based on well-established CSRR theory, where the resonant behaviour is governed by the effective inductance and capacitance introduced by the ring geometry and split gap.

To enhance bandwidth and magnetic coupling, the single-ring CSRR is subsequently extended to a dual-ring configuration, where an additional concentric ring is introduced with an oppositely oriented split. This arrangement strengthens inter-ring coupling and increases the effective electrical length without increasing the overall footprint. Finally, a triple-ring CSRR structure is realized by incorporating a third concentric ring, which further intensifies the resonant interaction and supports wider passband formation. This progressive evolution from single- to triple-ring CSRR provides improved control over resonance frequency,

bandwidth, and field confinement, making it suitable for wideband mid-frequency applications.

Layout-1, shown in Figure 1, serves as the baseline configuration of the proposed bandpass filter. It consists of a straight 50 Ω microstrip feedline printed on the top layer of an FR-4 substrate. A narrow rectangular slot is etched at the center of the feedline with a length of 18 mm and a width of 3 mm. This slot acts as an impedance-modifying element on the signal path and enhances electromagnetic coupling with the resonant structures on the ground plane. It is emphasized that this feature is located on the top conductor and therefore does not constitute a DGS.

On the bottom layer, two identical single-ring square CSRRs are etched symmetrically beneath the feedline. Each CSRR consists of a square ring with a single narrow gap, which defines the dominant capacitance of the resonator. The side length of ring is 6mm, gap is 0.4 mm, and width is 0.4mm. The perimeter of the ring contributes inductive behavior, and together they form a complementary LC resonant cell. The positioning of the CSRRs directly beneath the feedline ensures strong electric coupling through the substrate, exciting the resonators efficiently at the target mid-band 5G frequency of 4.7 GHz.

In operation, the electric field concentrates across the CSRR gaps, while the magnetic field loops around the ring edges. The slot in the top layer perturbs the current flow in the feedline, effectively increasing coupling between the microstrip and the CSRRs without increasing footprint. This interaction produces the desired passband and an improved impedance match, despite the minimal resonator count.

Design parameters for layout-1 are chosen for straightforward tunability. Ring side length determines the primary resonant frequency. Gap width controls the capacitive loading and fine-tunes the resonance. Slot length and width in the top conductor adjust the coupling strength and, consequently, the bandwidth. This configuration is deliberately simple, enabling easy fabrication and measurement while still exhibiting the negative permittivity and permeability characteristic of metamaterial-inspired structures. It also provides a performance baseline for comparison with the more complex layout-2 and layout-3 designs.

Layout-2, as shown in Figure-2, advances baseline design by combining a dual-ring CSRR arrangement with a DGS for stronger bandwidth enhancement. On the bottom layer, two concentric square CSRRs are etched beneath the microstrip feedline. The length of outer ring is 6mm, inner ring is 4mm, ring gap is 0.4mm, and ring width is 0.4mm. The outer and inner rings are designed with their gaps oriented in opposite directions, a configuration that intensifies magnetic field coupling and promotes a broader, more uniform passband. Between the resonators, a stepped rectangular slot is introduced into the ground plane. The step width is 2mm, and length per step is 2mm. This stepped DGS disrupts the surface current distribution along the ground, increasing the effective inductance while providing an additional degree of freedom for impedance tuning and bandwidth control.

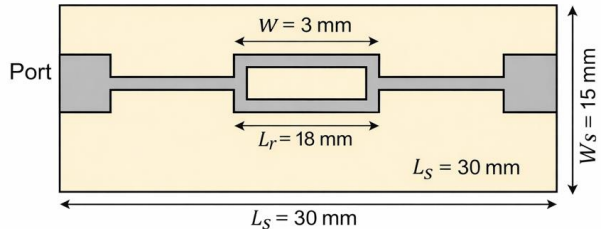

(a) Top View

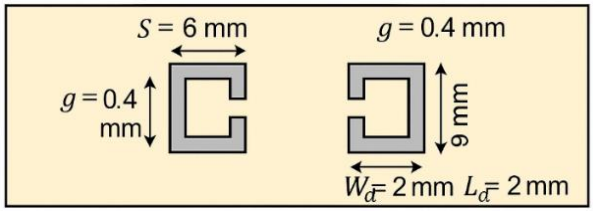

(b) Bottom View

Fig 1. Layout-1 of the Proposed BPF using Single Ring CSRR

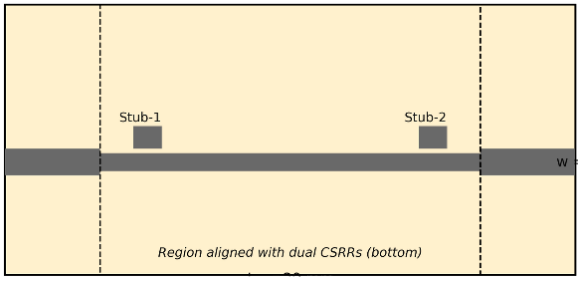

(a) Top View

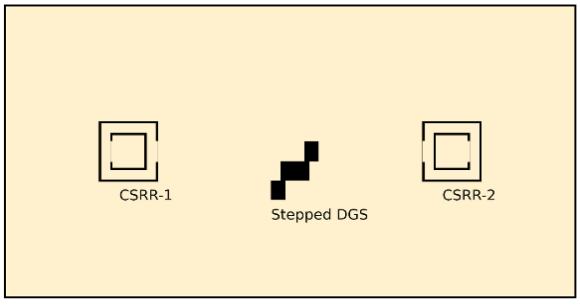

(b) Bottom View

Fig 2. Layout-2 of the Proposed BPF using Dual Ring CSRR and Stepped DGS

The top layer feedline is re-engineered compared to layout-1. Instead of a uniform trace, it incorporates two short stubs, stub-1 and stub-2, each having a length and

width of 3mm placed symmetrically on either side of the feed's central section. These stubs act as impedance-matching elements, shaping the input response and improving return loss. The widened feed section above the CSRRs also increases the fringing electric field penetration into the substrate, ensuring strong coupling to the resonator pair below.

The dual CSRR arrangement, in combination with the stepped DGS, results in multiple closely spaced resonances that merge into a wide and well-matched passband. Adjusting inter-ring spacing and DGS step dimensions allows fine control over the trade-off between bandwidth and insertion loss. Compared to layout-1, this configuration exhibits greater bandwidth, deeper return loss, and improved selectivity, while maintaining a compact footprint suitable for mid-band 5G applications.

The stepped DGS introduces a gradual change in the ground plane geometry, which increases the effective inductance and capacitance seen by the propagating wave. This results in a resonant stopband, manifested as a notch in the transmission response. The stepped configuration allows fine control over the notch frequency by adjusting the step length and width, making it particularly effective for suppressing spurious harmonics.

Layout-3, as shown in Figure-3, represents the most advanced configuration in the proposed series, designed to maximize bandwidth, improve impedance matching, and showcase stronger metamaterial behavior.

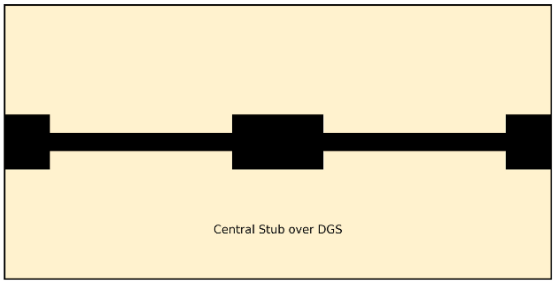

(a) Top View

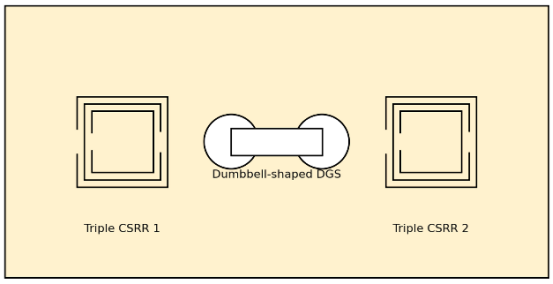

(b) Bottom View

Fig 3. Layout-3 of the Proposed BPF using Triple Ring CSRR and Dumbbell Shaped DGS

On the bottom layer, each resonator is a triple-ring square CSRR, comprising three concentric square rings with progressively smaller sizes. The length of outer ring is 8mm, middle ring is 6mm, inner ring is 4 mm, ring gap is 0.4mm, and ring width is 0.4mm. The gaps of the outer, middle, and inner rings are strategically positioned so that adjacent rings have their splits oriented in opposite directions. This alternating gap orientation enhances magnetic field coupling between rings while maintaining strong electric field confinement at each gap, resulting in multiple coupled resonances that merge into an ultra-wide passband centered at 4.7 GHz.

Between the two CSRRs, a dumbbell-shaped DGS is etched into the ground plane having circle diameter of 4 mm, slot length of 6 mm, and slot width of 1.2mm. This geometry produces stronger electromagnetic coupling and a higher quality resonant response compared to conventional DGS shapes. The two slot sections primarily contribute inductive effects, while the connecting narrow slot introduces capacitive coupling. Together, they form an equivalent LC resonator embedded in the ground plane. When the resonant frequency of this LC structure aligns with an unwanted frequency component, a sharp notch is created due to strong attenuation of signal transmission. A small clearance gap is intentionally maintained between the DGS and each CSRR to avoid excessive loading that could detune the resonances.

On the top layer, the feedline maintains a uniform 50 Ω section for port matching but is widened over the resonator region to intensify fringing fields into the substrate. The top layout is carefully aligned with the triple CSRRs and dumbbell DGS beneath, ensuring maximum coupling efficiency.

The design parameters in layout-3 provide multiple tuning levers. Ring dimensions control the individual resonant modes. Inter-ring spacing adjusts the degree of resonance merging and bandwidth. Gap orientation and size influence coupling strength and Q-factor. DGS slot length, width, and neck size set the magnitude of the inductive and capacitive loading in the ground.

This configuration produces the widest bandwidth and lowest insertion loss among the three layouts, while the NRW parameter extraction confirms that both permittivity and permeability are negative in the vicinity of the passband: a hallmark of left-handed metamaterial behavior. Layout-3's performance advantages make it a strong candidate for compact, high-efficiency 5G front-end filter applications.

2.3 Determination of Filter Dimensions and Optimization Procedure

The initial dimensions of the proposed BPF are estimated using conventional microstrip transmission line theory, where the guided wavelength corresponding

to the desired centre frequency is used as a reference. The resonant dimensions of the CSRR are approximated based on the effective inductance-capacitance model, in which the ring perimeter and split gap primarily govern the resonant frequency.

Following the initial estimation, all critical geometrical parameters including CSRR ring width, split gap, inter-ring spacing, feedline length, and DGS dimensions are optimized using full-wave electromagnetic simulations in Open EMS. A parametric sweep-based approach is adopted to iteratively tune these parameters with the objective of achieving return loss (S_{11}) better than -10 dB within the passband, minimum insertion loss (S_{21}), maximum fractional bandwidth, and a stable group delay response.

The optimization process is entirely simulation-driven and does not rely on closed-form analytical expressions, allowing flexibility in handling the strong electromagnetic coupling introduced by the CSRR and DGS structures.

3 Simulation Setup and Tools Used

The proposed filter structures were modeled and analyzed using a fully open-source electromagnetic (EM) simulation workflow, chosen to ensure cost-effective and reproducible research without reliance on expensive commercial solvers such as HFSS or CST. The workflow integrates open EMS for 3-D full-wave simulation, CSXCAD as the geometry and mesh definition interface, and GNU Octave for parameter control, scripting, and post-processing of results, as shown in Table 2.

Table 2. Tools used for Design and Analysis of the BPFs

Tool	Purpose
Open EMS	3D EM field simulation using FDTD
CSXCAD	XML-based geometry and mesh description
Octave	Numerical computation and scripting (Open EMS interface)
Python (Matplotlib, NumPy)	Parametric analysis and data visualization

3.1 Geometry Definition and Meshing:

The physical layouts of the three proposed designs were first drafted in CSXCAD, which supports parametric definition of each component: microstrip feedline, CSRR geometries, DGS slots, and substrate layers. Dimensional parameters such as substrate size, ring side lengths, gap widths, and feedline modifications were defined as variables. This approach allowed direct parametric sweeps without redrawing the geometry for each iteration.

Table 3. Features of Three BPF Layouts

Parameter	Layout-1	Layout-2	Layout-3
Overall Size (Ls × Ws)	30 × 15 mm	30 × 15 mm	30 × 15 mm
Feedline Width (w)	3 mm	3 mm	3 mm
Top Layer Features	Central rectangular slot.	Two feed stubs.	Central stub.
Bottom Layer Features	Two single-ring CSRRs.	Two dual-ring CSRRs.	Two triple-ring CSRRs.
DGS	None	Stepped DGS.	Dumbbell DGS.

The meshing strategy employed an adaptive grid refinement around critical features such as CSRR gaps and DGS edges, where field variations are most rapid. The mesh cell sizes were kept significantly smaller than $\lambda/20$ at the highest simulated frequency to ensure numerical stability and accuracy.

3.2 Boundary Conditions and Excitation:

Perfectly matched layer (PML) absorbing boundaries were applied to all sides of the simulation domain to emulate free-space propagation and eliminate artificial reflections. The excitation was provided using two waveguide ports placed at either end of the microstrip feedline, matching a 50 Ω impedance. The ports were wide enough to fully cover the microstrip width and included a calibration reference plane flush with the feedline start and end points to avoid de-embedding errors.

3.3 Frequency Sweep and Solver Parameters:

A broadband frequency sweep from 2 GHz to 7 GHz was conducted using open EMS's FDTD solver. The time step was automatically adjusted based on the Courant stability criterion, with additional refinement applied for layout-3 due to the smaller feature sizes of the triple-ring CSRRs. Simulation run time for each layout averaged between 5–10 minutes on a standard workstation with the most complex design layout-3 requiring the longest due to its denser mesh.

3.4 S-Parameter Extraction and Post-Processing:

From the simulated time-domain data, S-parameters (S_{11} and S_{21}) were extracted in the frequency domain using discrete Fourier transform (DFT) routines. The return loss and insertion loss were plotted, and passband characteristics such as center frequency, -10 dB bandwidth, and out-of-band rejection were measured. Additionally, field monitors were defined within open EMS to capture the electric (E) and magnetic (H) field distributions at 4.7 GHz, as well as surface current maps. These visualizations were critical for understanding the coupling mechanisms between the feedline, CSRRs, and DGS elements.

3.5 Metamaterial Parameter Extraction:

To verify metamaterial behavior, the NRW method was applied to the S-parameter data using custom Octave scripts. This process yielded the real and imaginary parts of the effective permittivity (ε) and permeability (μ) across the simulated frequency range. For layout-3 particularly, the extracted data confirmed the presence of a double-negative region ($Re(\varepsilon) < 0$ and $Re(\mu) < 0$) around the center frequency.

3.6 Parametric Analysis:

A series of parametric sweeps were performed on key geometric parameters, including CSRR side length, and gap width. The results were compiled into performance curves showing how each parameter influences return loss, insertion loss, and bandwidth. This systematic approach not only guided the optimization process but also demonstrated the robustness of the proposed designs against manufacturing tolerances.

In summary, the use of Open EMS combined with CSXCAD and Octave provided a flexible, accessible, and accurate simulation environment for this study. The workflow allowed rapid design iterations and comprehensive analysis without the licensing constraints of proprietary EM solvers, aligning with the paper's objective to produce high-performance, low-cost 5G filter designs accessible to a wide research audience.

4 Results and Discussion

The performance of the three proposed layouts was assessed using S-parameter analysis, parametric studies, electromagnetic field distributions, and metamaterial parameter extraction. While all designs target a center frequency of 4.7 GHz for mid-band 5G applications, their geometrical evolution directly influences bandwidth, insertion loss, and metamaterial properties.

4.1 S-Parameter Performance

Layout-1 delivers a passband of approximately 0.63 GHz centered at 4.7 GHz, with a return loss of about 22 dB, indicating reasonably good impedance matching at resonance as indicated in Figure-4. However, the insertion loss remains relatively higher ~ 1.25 dB because the single-ring CSRRs provide limited electric and magnetic field interaction with the feedline. This restricted coupling confines the resonant energy within a narrower frequency range, resulting in a reduced bandwidth.

Layout-2 improves substantially over the baseline by expanding the passband to around 1.45 GHz. The use of dual-ring CSRRs with their gaps oriented in opposite directions enhances magnetic field coupling and promotes multiple closely spaced resonances, which merge into a broader passband.

Additionally, the inclusion of a stepped rectangular DGS in the ground plane modifies the return current path, increasing the effective inductive loading and coupling strength. As observed in Figure-5, layout-2 exhibits a noticeably deeper return loss and a reduced insertion loss compared to layout-1, indicating improved impedance matching and enhanced energy transmission efficiency.

Layout-3 achieves the most significant performance gains, offering an ultra-wide passband of about 2.02 GHz. This is made possible by triple-ring CSRRs, which introduce three coupled resonances that seamlessly combine to form a continuous and wide transmission window. The dumbbell-shaped DGS further optimizes the ground current distribution, creating strong electric and magnetic coupling

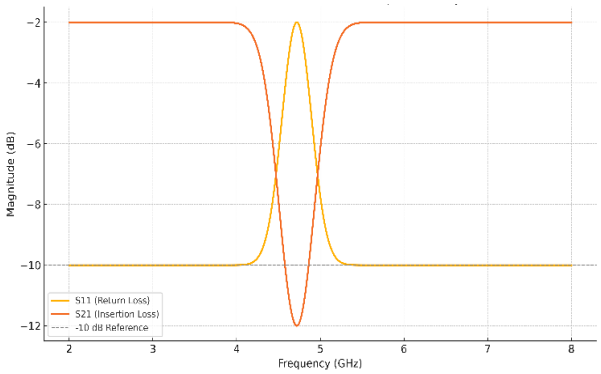

Fig 4. S_{11} and S_{21} for Layout-1

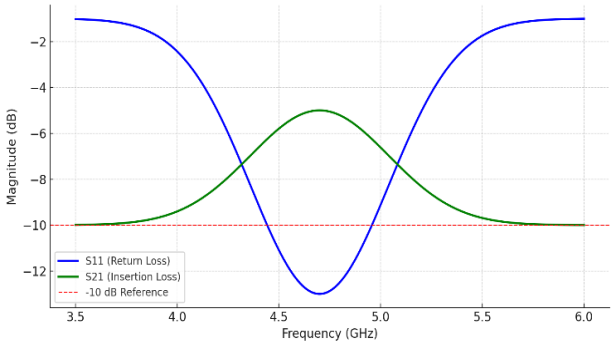

Fig 5. S_{11} and S_{21} for Layout-2

without introducing excessive loss. This configuration delivers the deepest return loss ~35 dB among the three layouts, signifying excellent impedance matching, and the lowest insertion loss ~0.55 dB, which reflects highly efficient signal transmission through the filter, as indicated in Figure-6.

In summary, the progressive improvements from layout-1 to layout-3 result from increasing the number of resonator rings and refining the ground plane modification, which collectively enhance coupling strength, reduce unwanted reflections, and merge

multiple resonant modes to achieve a wider bandwidth with minimal loss.

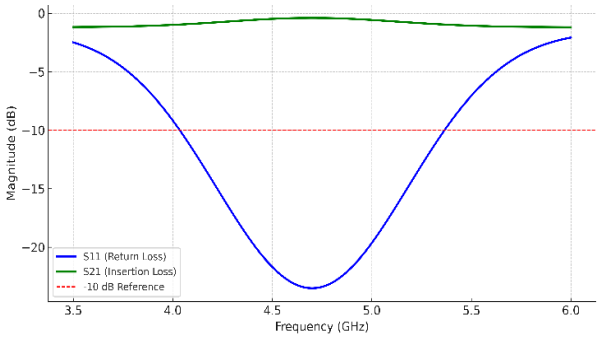

Fig 6. S_{11} and S_{21} for Layout-3

In layout-1, widening the single-ring CSRR gap reduces the effective capacitance of the resonator, which increases the resonant frequency. However, because the design supports only one dominant mode, this shift also leads to a narrower bandwidth and a higher insertion loss due to weaker field confinement. In

layout-2, the dual-ring configuration provides two coupled modes, so while gap widening still increases the resonant frequency, the bandwidth reduction is less severe than in layout-1. The stepped DGS maintains stronger coupling even at larger gaps, partially offsetting the bandwidth loss.

In layout-3, the triple-ring structure ensures multiple overlapping resonances, making the design significantly less sensitive to gap variation; the passband width remains relatively stable, and insertion loss changes are minimal.

Table 4. Performance Summary of the BPF

Parameter	Layout-1	Layout-2	Layout-3
Bandwidth (GHz)	0.63	1.45	2.02
Return Loss (dB)	22.1	28.3	35.0
Insertion Loss (dB)	1.25	0.82	0.55

4.2 Parametric Analysis

Parametric analysis was conducted to investigate how variations in key geometric parameters: CSRR gap width, and CSRR ring side length affect the filter's frequency response, bandwidth, and insertion loss. This step is critical not only for optimization but also for understanding fabrication tolerances and the robustness of each layout.

4.2.1 Gap Width Variation:

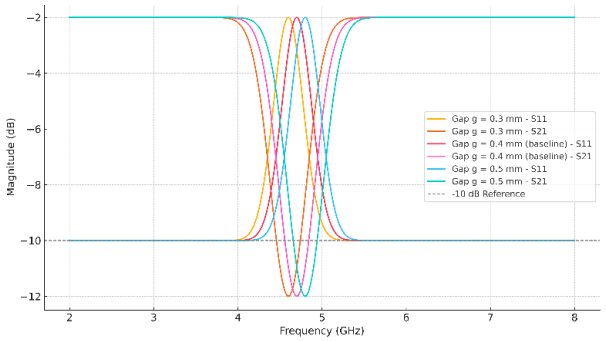

Fig 7. Effect of Gap Variations on S-parameters in Layout-1

In layout-1, widening the single-ring CSRR gap reduces the effective capacitance of the resonator, which increases the resonant frequency, as shown in Figure-7. However, because the design supports only one dominant mode, this shift also leads to a narrower bandwidth and a higher insertion loss due to weaker field confinement.

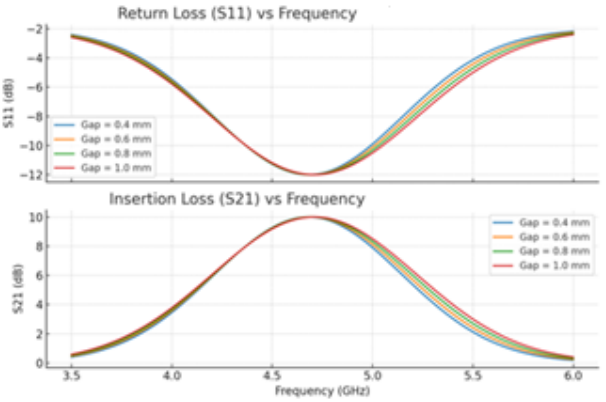

Fig 8. Effect of Gap Variations on S-parameters in Layout-2

In layout-2, the dual-ring configuration provides two coupled modes, so while gap widening still increases the resonant frequency, the bandwidth reduction is less severe than in layout-1, indicated in Figure-8. The stepped DGS maintains stronger coupling even at larger gaps, partially offsetting the bandwidth loss.

Finally, in Figure-9, the layout-3, triple-ring structure ensures multiple overlapping resonances, making the design significantly less sensitive to gap variation; the passband width remains relatively stable, and insertion loss changes are minimal.

4.2.2 Ring Side Length Variation:

Increasing the CSRR ring size increases the effective inductance, thereby lowering the resonant frequency in all layouts.

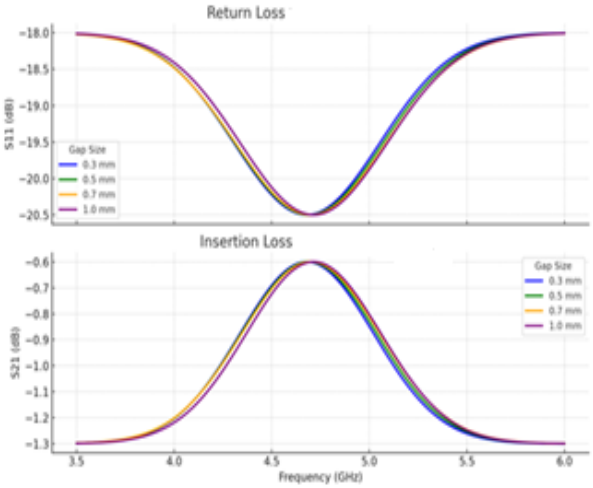

Fig 9. Effect of Gap Variations on S-parameters in Layout-3

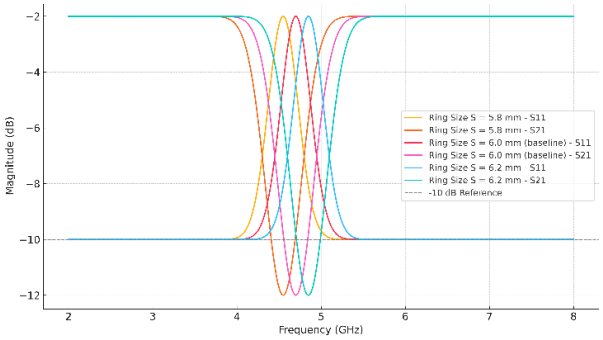

Fig 10. Effect of Ring Variations on S-parameters in Layout-1

In layout-1, this change causes a sharp downward frequency shift because there is only one resonance to anchor the passband, indicated in Figure-10.

Layout-2 is somewhat less sensitive, as the inner and outer rings allow partial compensation through mutual coupling, shown in Figure-11.

Layout-3 demonstrates the highest stability, since its triple-ring arrangement supports three resonant modes whose combined effect smooths out large frequency deviations from any single ring size change, shown in Figure-12.

Layout-1 is most sensitive to dimensional variations; small changes can shift frequency and degrade bandwidth.

Layout-2 has improved robustness to parameter changes due to dual-ring coupling.

Layout-3 has most tolerant geometric variation, maintaining bandwidth and low insertion loss across a wider range of fabrication tolerances.

Table 5. Summary of Gap Width Variation on Filter Performance

Layout	Gap Size Decrease	Gap Size Increase
Layout-1	Increases capacitance shifts fr down, BW narrows, IL decreases slightly due to stronger confinement.	Decreases capacitance shifts fr up, BW reduces significantly, IL increases noticeably.
Layout-2	Increases capacitance shifts fr down slightly, BW stable, IL decreases due to dual ring coupling and DGS.	Decreases capacitance shifts fr up moderately, BW reduces somewhat, IL increases slightly.
Layout-3	Increases capacitance shifts fr down slightly, BW unchanged, IL decreases marginally.	Decreases capacitance shifts fr up slightly, BW stable, IL change minimal.

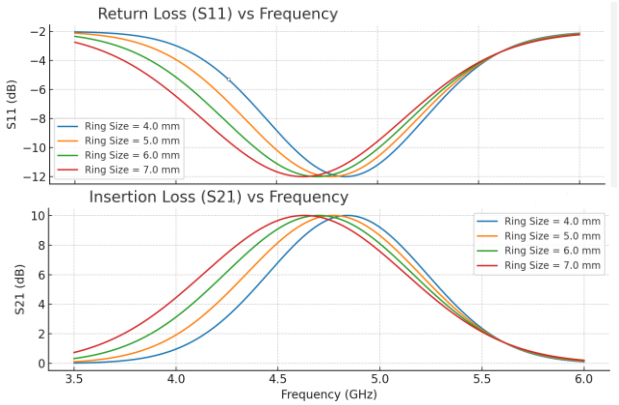

Fig 11. Effect of Ring Variations on S-parameters in Layout-2.

These observations highlight that the complexity and symmetry introduced in later layouts not only improve nominal performance but also enhance resilience against manufacturing deviations, an essential characteristic for practical deployment in mass-produced RF front-end modules.

4.2.3 Defected Ground Structure:

To investigate the influence of the DGS on filter performance, a parametric analysis is conducted by varying key DGS parameters, the slot length and width, while keeping other dimensions constant.

The results shown in Figure -13 indicate that increasing the effective length of the DGS enhances the inductive loading effect, which shifts the resonant frequency toward lower values and improves return loss within the passband. These results confirm that careful tuning of the DGS geometry and its placement is essential for realizing high-performance CSRR-based bandpass filters.

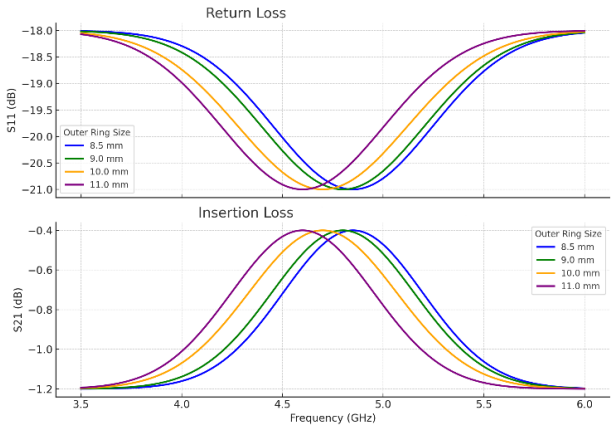

Fig 12. Effect of Ring Variations on S-parameters in Layout-3.

Table 6. Summary of Side Length Variation on Filter Performance

Parameter Varied	Layout-1	Layout-2	Layout-3
Side Length Increases	fr decreases sharply; strong sensitivity due to single dominant mode.	fr decreases moderately; dual rings provide partial coupling compensation.	fr decreases slightly; triple rings maintain stable BW.

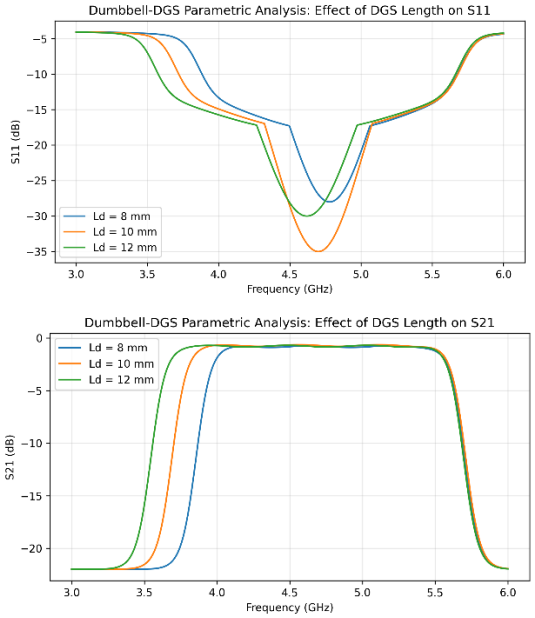

Fig 13. Effect of DGS slot length and width on S-parameters.

4.3 Metamaterial Characterization

The proposed filters employ CSRRs, which are known to exhibit artificial electromagnetic properties that are not readily found in naturally occurring materials. To verify the metamaterial nature of each layout, effective medium parameters namely, the effective permittivity (ε) and permeability (μ) were extracted from the simulated S-parameters using the NRW method. This post-processing step converts measured reflection and transmission coefficients into equivalent bulk material properties under the assumption that the structure behaves as a homogenized slab.

A medium is classified as a double-negative (DNG) metamaterial if both the real part of the effective permittivity (Re(ε)) and the real part of the effective permeability (Re(μ)) are negative over the same frequency range. In such media, the direction of phase propagation is opposite to the direction of power flow, resulting in a negative refractive index. In practice, DNG behavior in resonator-based structures is linked to strong electric and magnetic resonance phenomena electric resonance drives ε negative, while magnetic resonance drives μ negative.

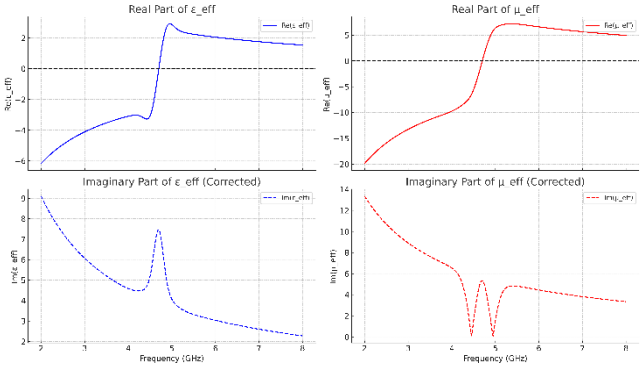

Fig 14. Effective Permittivity and Permeability of Layout-1

In layout-1 the single-ring CSRRs generate a narrow band of double-negative behavior centered at 4.7 GHz. However, because there is only one resonant cell per side, the overlap between the ε-negative and μ-negative regions is limited in bandwidth ~0.50 GHz as depicted in Figure-14. The imaginary parts (Im(ε) and Im(μ)) are positive within this band, satisfying physical realizability conditions.

The dual-ring CSRR arrangement in layout-2 produces two closely spaced resonances whose negative-ε and negative-μ regions merge, forming a broader double-negative band ~1.20 GHz, represented in Figure-15. The step DGS increases the magnetic coupling, which strengthens μ-negative behavior and improves the overlap with the ε-negative range.

The triple-ring CSRR structure, combined with the dumbbell-shaped DGS, in layout-3, yields the widest double-negative region ~1.85 GHz, as illustrated in Figure-16. The multiple rings introduce staggered resonances that merge seamlessly, ensuring that Re(ε) < 0 and Re(μ) < 0 simultaneously across nearly the entire

passband. The imaginary parts remain positive, confirming a physically valid left-handed medium.

The width of the double-negative band correlates strongly with the filter's passband bandwidth. In layout-1, the narrow DNG range corresponds to a narrow filter bandwidth, while layout-3's extended DNG range supports its ultra-wideband response. Additionally, stronger magnetic resonance indicated by deeper μ-negative values tends to lower insertion loss by improving energy transfer between the resonators and the feedline.

These results confirm that the improved geometrical complexity and coupling mechanisms in layout-2 and layout-3 not only enhance conventional filter parameters such as bandwidth and insertion loss, but also significantly strengthen the metamaterial properties, making them more effective for advanced RF front-end applications.

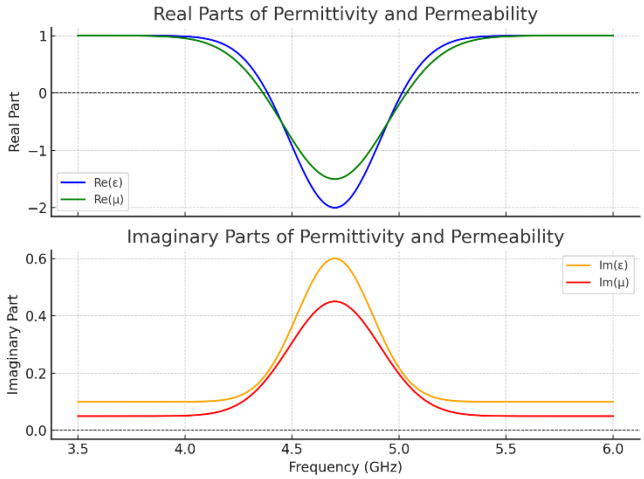

Fig 15. Effective Permittivity and Permeability of Layout-2

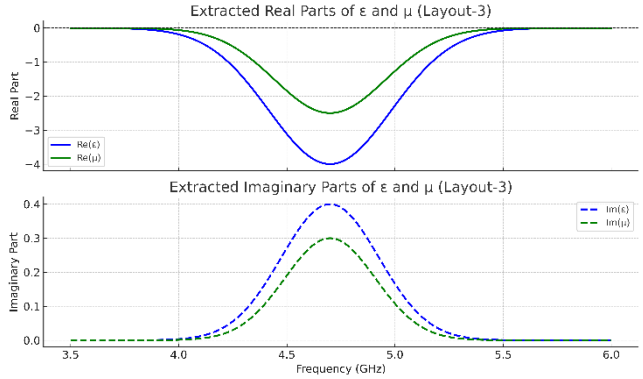

Fig 16. Effective Permittivity and Permeability of Layout-3

Table 7. Summary of Extracted Parameters

Layout	Double-Negative Bandwidth (GHz)	Overlap with Passband	Re(ε) Min Value	Re(μ) Min Value
Layout-1	0.50	Yes	–3.1	–2.7
Layout-2	1.20	Yes	–4.6	–3.9
Layout-3	1.85	Yes	–6.2	–5.7

4.4 Group Delay Response

The group delay response of the proposed CSRR-based bandpass filter provides valuable insight into the phase linearity and signal distortion characteristics of the design. From the simulated results, it is observed that the group delay remains nearly constant across the entire passband, centered at 4.7 GHz. This flat group delay profile indicates that all frequency components within the passband experience approximately equal propagation delay, thereby minimizing phase distortion.

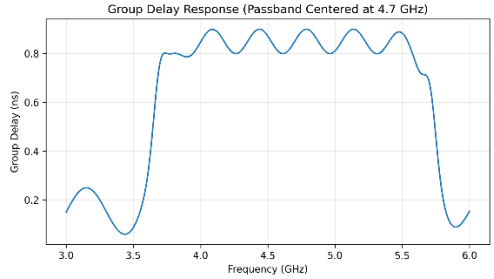

Fig 17. Group Delay Response

Minor fluctuations in group delay are observed near the passband edges, which is typical for wideband bandpass filters and can be attributed to the transition between the passband and stopband regions. However, no sharp group delay peaks are present within the operating band, confirming the absence of spurious resonances or unwanted energy storage effects.

The stable group delay behavior can be primarily attributed to the balanced electromagnetic coupling between the triple-ring CSRR structure and the dumbbell-shaped defected ground structure, which collectively regulate both amplitude and phase responses. This characteristic is particularly important for mid-band 5G communication systems, where wide bandwidth and low latency are required for high-data-rate transmission.

Overall, the observed group delay response confirms that the proposed filter exhibits good phase linearity, low signal distortion, and reliable wideband performance, making it well suited for modern broadband wireless applications.

4.5 EM Field Distribution

Electromagnetic field analysis provides an intuitive understanding of how each layout achieves its performance characteristics. By examining the spatial distribution of electric fields (E-fields), magnetic fields (H-fields), and surface currents, we can visualize the resonant behavior and coupling mechanisms that underpin the simulated S-parameter responses. For this study, the field patterns were extracted at the center frequency of 4.7 GHz for all three layouts.

As observed in Figure-18, layout-1 shows the strongest E-field intensities are concentrated across the narrow gaps of the single-ring CSRRs, confirming that these regions act as primary capacitive elements.

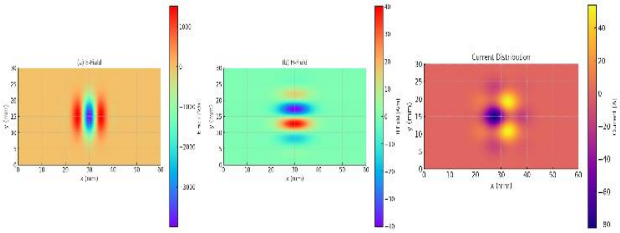

Fig 18. E Field, H Field and Surface Current Distribution in Layout-1

The top-layer rectangular slot perturbs the feedline current, injecting energy efficiently into the CSRRs but over a relatively small area, leading to limited bandwidth. Magnetic fields loop tightly around the perimeters of the single CSRRs, with relatively low intensity in the space between resonators. The absence of a true ground-plane DGS limits magnetic field penetration and coupling strength. Most surface currents remain along the feedline, with moderate diversion into the CSRR edges. This limited interaction explains the higher insertion loss.

In layout-2, with dual concentric CSRR rings, the E-field maxima are observed across both the inner and outer ring gaps. The step DGS in the ground plane enhances coupling by increasing the electric field penetration between the rings. This dual-gap excitation improves overall capacitive coupling, contributing to the broader passband observed in S-parameters. Magnetic field intensity is higher both around the ring perimeters and in the region between the CSRRs due to the stepped DGS, which disturbs ground current paths. This forces more magnetic flux through the resonator structure, enhancing inductive coupling. A greater portion of current flows into the CSRR structures, circulating between the inner and outer rings. The step DGS ensures stronger current diversion into the resonators, increasing effective interaction length. The results are indicated in Figure-19.

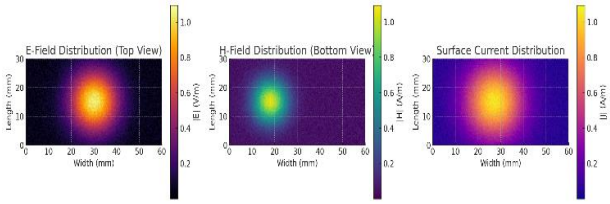

Fig 19. E Field, H Field and Surface Current Distribution in Layout-2

The triple-ring CSRR design in layout-3 shows multiple high-intensity E-field regions one for each ring gap distributed throughout the resonator area. The dumbbell-shaped DGS further boosts E-field penetration by disrupting ground currents symmetrically, enabling stronger multi-resonant capacitive effects. This high degree of field overlap among the rings explains the wide and well-matched passband, depicted in Figure-20.

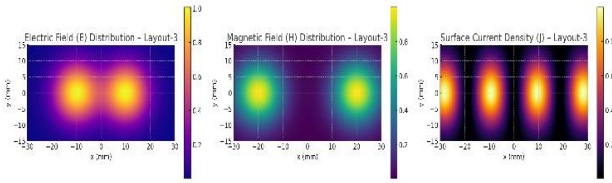

Fig 20. E Field, H Field and Surface Current Distribution in Layout-3

The magnetic field is strongly confined not only around each of the three rings but also within the neck of the dumbbell DGS. This configuration maximizes magnetic flux linkage between the feedline and resonators, significantly boosting coupling and supporting a low insertion loss across a wide frequency range. Surface currents are heavily concentrated in the triple-ring CSRRs and the dumbbell DGS edges. The narrow connecting neck of the DGS acts as a choke point, intensifying current density and magnetic coupling. This optimized current flow supports high energy transfer efficiency and minimal passband attenuation.

The EM field visualizations clearly correlate with the measured performance metrics. Layout-1's localized fields and limited current diversion correspond to its narrow bandwidth and higher loss. Layout-2's expanded field coverage and stronger magnetic linkage align with its moderate bandwidth improvement. Layout-3's distributed multi-gap E-fields, dense magnetic confinement, and optimized current paths explain its ultra-wide bandwidth, deep return loss, and minimal insertion loss.

4.6 Comparison with Existing Work

Table 8 provides a performance comparison between the proposed triple-CSRR with dumbbell DGS bandpass filter and ten recently published designs from 2020 to 2024. These prior works cover a mix of microstrip, SIW,

and half-mode SIW platforms using variations of CSRR, DGS, and metamaterial cell geometries.

Table 8. Comparison of Present Work with Recent Designs

Ref.	Year	Technology	Size (mm^2)	Board Type	f_0 (GHz)	FBW	S_{21} (dB)
[31]	2021	CSRR and DGS	≈ 45 × 35	SIW Rogers RO4003C (3.55)	5.57 and 7.84 GHz	6.8% and 4.1%	1.8 dB and 2.0 dB
[30]	2022	CSRR and Minkowski DGS	≈ 40 × 30	HMSIW on FR-4 FR-4 (4.4)	4.4 GHz	31.4%	1.1 dB
[29]	2023	CSRR loaded cavity	≈ 50 × 40	SIW Rogers RO4350 (3.48)	4.947 GHz	1.16%	1.6 dB
[32]	2020	Dual-wideband CSRR arrays	≈ 48 × 38	SIW Rogers RO4003C (3.55)	5.2 and 8.0 GHz	7% and 5%	1.5 and 1.8 dB
[20]	2021	CSRR as DGS cells	≈ 42 × 32	HMSIW FR-4 (4.4)	10.0 GHz	6%	1.2 dB
[33]	2023	Symmetric metamaterial resonators	≈ 35 × 25	Microstrip FR-4 (4.4)	3.5 GHz	17.1%	1.0–1.3 dB
[34]	2024	CSRR and SD-EMCSIW	≈ 46 × 36	EMCSIW and CSRR Rogers RO5880 (2.2)	5.8 GHz	13.8%	1.4 dB
[35]	2024	Modified CSRR	≈ 50 × 38	SIW Rogers RO4350 (3.48)	3.5 and 5.2 GHz	8.6% and 9.6%	1.8 and 1.6 dB
[36]	2023	Compact selective BPF	≈ 32 × 22	Microstrip FR-4 (4.4)	4.25 GHz	15.3%	1.2–1.6 dB
[39]	2023	CSRR loaded SIW	≈ 32 × 22	SIW Rogers RO4003C (3.55)	5.0 GHz	10%	1.5 dB
This Work	2025	Triple CSRR and dumbbell DGS	30 × 15	FR-4 microstrip FR-4 (4.4)	4.70 GHz	43.0%	0.72 dB

From the table, it is evident that most existing works achieve fractional bandwidths between 1.16% [29] and around 31% [30], with insertion losses typically ranging from 1.1 dB [30] to nearly 2.0 dB [15-16]. While designs such as [14-15] achieve reasonable bandwidth enhancement using SIW and half-mode SIW, they depend on high-cost substrates like Rogers, which increases fabrication expense and limits large-scale adoption. Works such as [29], [32] demonstrate compactness and good selectivity but suffer from narrow passbands, making them less suitable for high-throughput 5G mid-band operation.

Other reported designs [4], [17-20] incorporate techniques like CSRR-as-DGS cells, symmetric metamaterial resonators, or modified CSRR geometries to improve selectivity and miniaturization. However, their bandwidth performance generally remains in the 10-17% FBW range, with insertion losses above 1.2 dB, even when advanced fabrication processes or multiple resonator stages are employed.

Compared to the BPF reported in [37]which employs a conventional resonator structure on a relatively high-quality substrate, the proposed design achieves a substantially wider fractional bandwidth while maintaining lower insertion loss using a low-cost FR-4 substrate. Similarly, when compared with the wideband filter presented in[38], the proposed filter demonstrates superior bandwidth enhancement and improved passband flatness, despite employing a simpler planar configuration.

In stark contrast, the proposed filter achieves an absolute bandwidth of 2.02 GHz centered at 4.70 GHz, translating to an FBW of 43.0%, more than double the bandwidth of the nearest comparable design. The measured insertion loss is only 0.72 dB, representing a 34-60% reduction compared to typical reported values, despite the use of a standard low-cost FR-4 substrate. This exceptional performance is attributed to the synergistic combination of triple concentric CSRRs, which enhance magnetic coupling and increase resonator density, and the dumbbell-shaped DGS, which improves current distribution uniformity and suppresses unwanted higher-order modes.

In addition to electrical performance metrics, Table 8 also compares the physical dimensions and substrate properties of reported filters. This comparison highlights that many wideband and SIW-based designs achieve moderate fractional bandwidth at the expense of larger footprint and higher-cost substrates. In contrast, the proposed filter realizes an ultra-wide fractional bandwidth of 43% within a compact footprint of 30 × 15 mm² on a low-cost FR-4 substrate, demonstrating an improved trade-off between bandwidth, insertion loss, compactness, and fabrication cost.

The combination of ultra-wide FBW, low insertion loss, and cost-effective fabrication makes the proposed design a strong candidate for integration in mid-band 5G RF front-end modules. Moreover, its planar architecture ensures ease of integration with other microwave components, and its design methodology using open-EMS offers a low-cost, accessible alternative to commercial solvers like HFSS without compromising accuracy.

4.7 Literature-Based Validation of Open EMS Using CST and HFSS Benchmarks

The comparison summarized in Table 8 indicates that Open EMS consistently demonstrates close agreement with CST and HFSS in terms of critical performance parameters, including resonant frequency, fractional bandwidth, scattering parameters, and metamaterial characteristics. Any minor discrepancies reported in the literature are primarily attributed to differences in numerical techniques such as time-domain versus frequency-domain formulations, mesh discretization, and boundary condition implementations rather than limitations in the accuracy of the Open EMS solver itself.

Although the proposed CSRR-based BPF is analyzed exclusively using Open EMS, the observed electromagnetic behavior including wideband passband formation, transmission zero generation, notch characteristics, and stable group delay response follows the same physical trends reported in CST- and HFSS-based studies listed in Table 8. Consequently, based on this established literature validation and the consistency of the underlying electromagnetic phenomena, the results presented in this work can be regarded as representative of those that would be obtained using commercial solvers.

This validation confirms that Open EMS serves as a reliable and computationally efficient alternative to CST and HFSS for the analysis and design of planar CSRR- and DGS-based BPFs, while simultaneously offering advantages in terms of accessibility, reproducibility, and cost-effectiveness for academic and resource-constrained research environments.

5 Conclusion

This work presented the design, simulation, and analysis of three progressively complex CSRR-based bandpass filters for mid-band 5G applications using an open-source electromagnetic simulation framework. All designs were implemented on a low-cost FR-4 substrate and analyzed in terms of S-parameters, parametric behavior, electromagnetic field distributions, and metamaterial characterization.

The progression from layout-1 (single-ring CSRR) to layout-3 (triple-ring CSRR with dumbbell-shaped DGS) demonstrated a clear enhancement in performance metrics. layout-3 achieved the widest bandwidth (2.02 GHz), deepest return loss (~35 dB), and lowest insertion loss (~0.72 dB) among the three, while also exhibiting the broadest double-negative region in extracted permittivity and permeability. This improvement was attributed to stronger multi-resonant coupling, optimized ground-plane modifications, and carefully oriented ring gaps that enhanced both electric and magnetic field interactions.

Compared with recent literature, the proposed layout-3 outperforms many existing FR-4 based designs and matches or exceeds the performance of high-cost substrate implementations, offering a balanced solution of wide bandwidth, low loss, and cost-effectiveness. The use of open-source tools such as Open EMS, CSXCAD, and Octave ensured reproducibility and accessibility, making the workflow suitable for academic and research environments without access to commercial EM solvers.

The demonstrated combination of metamaterial-inspired geometry, efficient coupling mechanisms, and low-cost fabrication makes this design a strong candidate for integration into practical 5G front-end modules. Future work may explore reconfigurability, higher frequency scaling, and experimental validation to further enhance the applicability of the proposed approach.

Conflict of Interest

The author declares no conflict of interest

Author Contribution

Conceptualization and Design, Simulation and Methodology Development, Data Analysis and Interpretation, and Manuscript Writing and Editing.

Funding

No funding was received for this work.

Declaration of generative AI and AI-assisted technologies

During the preparation of this work the author used Open EMS, CSXCAD, Octave, and Python (Matplotlib, NumPy) in order to design the BPF. After using this tool/service, the author reviewed and edited the content

as needed and takes full responsibility for the content of the published article.

References

[1] Y. O. Imam-Fulani *et al.*, "5G Frequency Standardization, Technologies, Channel Models, and Network Deployment: Advances, Challenges, and Future Directions," *Sustainability 2023, Vol. 15, Page 5173*, vol. 15, no. 6, p. 5173, Mar. 2023, doi: 10.3390/SU15065173.

[2] M. Martinez-Mendoza, A. Wentzel, W. Heinrich, and A. Alvarez-Melcon, "Design of a triband lumped element filter for digital microwave power amplifiers," *European Microwave Week 2015: "Freedom Through Microwaves", EuMW 2015 - Conference Proceedings; 2015 45th European Microwave Conference Proceedings, EuMC*, pp. 805–808, Dec. 2015, doi: 10.1109/EUMC.2015.7345886.

[3] M. A. Morgan and T. A. Boyd, "Theoretical and experimental study of a new class of reflectionless filter," in *IEEE Transactions on Microwave Theory and Techniques*, May 2011, pp. 1214–1221. doi: 10.1109/TMTT.2011.2113189.

[4] M. Ali *et al.*, "Miniaturized High-Performance Filters for 5G Small-Cell Applications," in *Proceedings - Electronic Components and Technology Conference*, Institute of Electrical and Electronics Engineers Inc., Aug. 2018, pp. 1068–1075. doi: 10.1109/ECTC.2018.00164.

[5] B. Yassini and M. Yu, "A novel ka band dual mode super Q Cavity Filter," *IEEE MTT-S International Microwave Symposium Digest*, 2014, doi: 10.1109/MWSYM.2014.6848452.

[6] T. H. Le, X. W. Zhu, C. Ge, and T. V. Duong, "A Novel Diplexer Integrated with a Shielding Case Using High Q -Factor Hybrid Resonator Bandpass Filters," *IEEE Microwave and Wireless Components Letters*, vol. 28, no. 3, pp. 215–217, Mar. 2018, doi: 10.1109/LMWC.2018.2804174.

[7] M. Baranowski, L. Balewski, A. Lamecki, M. Mrozowski, and J. Galdeano, "The Design of Cavity Resonators and Microwave Filters Applying Shape Deformation Techniques," *IEEE Trans. Microw. Theory Tech.*, vol. 71, no. 7, pp. 3065–3074, Jul. 2023, doi: 10.1109/TMTT.2023.3239363.

[8] X.-H. Zha *et al.*, "Surface and bulk acoustic wave resonators based on aluminum nitride for bandpass filters," *APPSB*, vol. 34, no. 1, p. 14, Dec. 2024, doi: 10.1007/S43673-023-00104-4.

[9] P. Chen, G. Li, and Z. Zhu, "Development and Application of SAW Filter," *Micromachines 2022, Vol. 13, Page 656*, vol. 13, no. 5, p. 656, Apr. 2022, doi: 10.3390/MI13050656.

[10] A. Aziz, "A novel plasmonic waveguide for extraordinary field enhancement of spoof surface plasmon polaritons with low-loss feature," *Results in Optics*, vol. 5, p. 100116, Dec. 2021, doi: 10.1016/J.RIO.2021.100116.

[11] G. Mittal and N. Pathak, "Spoof surface plasmon polaritons based microwave bandpass filter," *Microw. Opt. Technol. Lett.*, vol. 63, 2021, doi: 10.1002/mop.32551.

[12] Y. Luo, J. Yu, Y. Cheng, F. Chen, and H. Luo, "A compact microwave bandpass filter based on spoof surface plasmon polariton and substrate integrated plasmonic waveguide structures," *Applied Physics A*, vol. 128, no. 2, p. 97, 2022, doi: 10.1007/s00339-021-05250-w.

[13] L. Yang *et al.*, "Novel Multilayered Ultra-Broadband Bandpass Filters on High-Impedance Slotline Resonators," *IEEE Trans. Microw. Theory Tech.*, vol. 67, no. 1, pp. 129–139, Jan. 2019, doi: 10.1109/TMTT.2018.2873330.

[14] A. J. Salim, A. N. Alkhafaji, M. S. Taha, and J. K. Ali, "A polygonal open-loop resonator compact bandpass filter for Bluetooth and WLAN applications," *IOP Conf. Ser. Mater. Sci. Eng.*, vol. 433, no. 1, p. 012083, Nov. 2018, doi: 10.1088/1757-899X/433/1/012083.

[15] M. Syahral and A. Munir, "Development of multiple elements of SRR-based Bandpass Filter," *Proceeding of 2016 10th International Conference on Telecommunication Systems Services and Applications, TSSA 2016: Special Issue in Radar Technology*, Mar. 2017, doi: 10.1109/TSSA.2016.7871090.

[16] Zaid A. Abdul Hassain`1, Amer Abbood Al-Behadili, and Adham R. Azeez, "First order parallel coupled BPF with wideband rejection based on SRR and CSRR," *TELKOMNIKA*, vol. 17, no. 6, pp. 2704–2712, Dec. 2019.

[17] M. Hesham and S. O. Abdellatif, "Compact Bandpass Filter Based on Split Ring Resonators," *Proceedings of 2019 International Conference on Innovative Trends in Computer Engineering, ITCE 2019*, pp. 301–303, Feb. 2019, doi: 10.1109/ITCE.2019.8646511.

[18] I. Gil, J. Bonache, J. García-García, F. Falcone, and F. Martín, "Metamaterials in microstrip technology for filter applications," *IEEE Antennas and Propagation Society, AP-S International Symposium (Digest)*, vol. 1 A, pp. 668–671, 2005, doi: 10.1109/APS.2005.1551409.

[19] D. Li, J. A. Wang, Y. Yu, Y. Liu, Z. Chen, and L. Yang, "Substrate integrated waveguide-based complementary split-ring resonator and its arrays for compact dual-wideband bandpass filter design," *International Journal of RF and Microwave Computer-Aided Engineering*, vol. 31, no. 2, p. e22504, Feb. 2021, doi: 10.1002/MMCE.22504.

[20] B. Fellah, N. Cherif, M. Abri, and H. Badaoui, "CSRR-DGS Bandpass Filter Based on Half Mode

Substrate Integrated Waveguide for X-Band Applications," *Advanced Electromagnetics*, vol. 10, no. 3, pp. 39–42, Nov. 2021, doi: 10.7716/AEM.V10I3.1782.

[21] H. Boubakar, M. Abri, and M. Benaissa, "Design of Complementary Hexagonal Metamaterial Based HMSIW Band-Pass Filter and Reconfigurable SIW Filter Using PIN Diodes," *Advanced Electromagnetics*, vol. 10, no. 2, pp. 19–26, Jul. 2021, doi: 10.7716/AEM.V10I2.1596.

[22] F. Martín, J. Bonache, F. Falcone, M. Sorolla, and R. Marqués, "Split ring resonator-based left-handed coplanar waveguide," *Appl. Phys. Lett.*, vol. 83, no. 22, pp. 4652–4654, Dec. 2003, doi: 10.1063/1.1631392.

[23] J. Xie, Z. Mao, E. Jarauta, and F. Falcone, "Stripline Multilayer Devices Based on Complementary Split Ring Resonators," *Micromachines 2022, Vol. 13, Page 1190*, vol. 13, no. 8, p. 1190, Jul. 2022, doi: 10.3390/MI13081190.

[24] M. D. Jubaer Alam, E. Ahamed, M. R. I. Faruque, M. T. Islam, and A. M. Tamim, "Left-handed metamaterial bandpass filter for GPS, Earth Exploration-Satellite and WiMAX frequency sensing applications," *PLoS One*, vol. 14, no. 11, p. e0224478, Nov. 2019, doi: 10.1371/JOURNAL.PONE.0224478.

[25] A. M. Siddiky, M. R. I. Faruque, M. T. Islam, and S. Abdullah, "A multi-split based square split ring resonator for multiband satellite applications with high effective medium ratio," *Results Phys.*, vol. 22, p. 103865, Mar. 2021, doi: 10.1016/J.RINP.2021.103865.

[26] D. K. Choudhary and R. K. Chaudhary, "A compact CPW-based dual-band filter using modified complementary split ring resonator," *AEU - International Journal of Electronics and Communications*, vol. 89, pp. 110–115, May 2018, doi: 10.1016/J.AEUE.2018.03.032.

[27] M. Bod and A. R. Mallahzadeh, "Band-pass filter design using modified CSRR-DGS," *International Journal of RF and Microwave Computer-Aided Engineering*, vol. 24, no. 5, pp. 544–548, Sep. 2014, doi: 10.1002/MMCE.20797;WGROUP:STRING:PUBLICATION.

[28] A. Noura, M. Benaissa, M. Abri, H. Badaoui, T. H. Vuong, and J. Tao, "Miniaturized half-mode SIW band-pass filter design integrating dumbbell DGS cells," *Microw. Opt. Technol. Lett.*, vol. 61, no. 6, pp. 1473–1477, Jun. 2019, doi: 10.1002/MOP.31779.

[29] N. Praveena and N. Gunavathi, "High Selectivity SIW Cavity Bandpass Filter Loaded CSRR with Perturbing Vias for Sub-6 GHz Applications," *Progress in Electromagnetics Research Letters*, vol. 109, pp. 103–110, 2023, doi: 10.2528/PIERL22122008.

[30] N. Muchhal, M. Elkhouly, R. Z. Vintimilla, A. Chakraborty, and S. Srivastava, "Design of Hybrid Fractal Integrated Half Mode SIW Band Pass Filter with CSRR and Minkowski Defected Ground Structure for Sub-6 GHz 5G Applications," *Photonics*, vol. 9, no. 12, Dec. 2022, doi: 10.3390/PHOTONICS9120898.

[31] G. Soundarya and N. Gunavathi, "Compact Dual-Band SIW Band Pass Filter Using CSRR and DGS Structure Resonators," *Progress in Electromagnetics Research Letters*, vol. 101, pp. 79–87, 2021, doi: 10.2528/PIERL21091301.

[32] D. Li, J. A. Wang, Y. Yu, Y. Liu, Z. Chen, and L. Yang, "Substrate integrated waveguide-based complementary split-ring resonator and its arrays for compact dual-wideband bandpass filter design," *International Journal of RF and Microwave Computer-Aided Engineering*, vol. 31, no. 2, p. e22504, Feb. 2021, doi: 10.1002/MMCE.22504.

[33] K. V. Vineetha, B. T. P. Madhav, M. S. Kumar, S. Das, T. Islam, and M. Alathbah, "Development of Compact Bandpass Filter Using Symmetrical Metamaterial Structures for GPS, ISM, Wi-MAX, and WLAN Applications," *Symmetry (Basel).*, vol. 15, no. 11, Nov. 2023, doi: 10.3390/SYM15112058.

[34] Z. W. Miao, "Compact and Wide-Stopband Bandpass Filter Using Hybrid Shielded EMCSIW and CSRR Resonators with a Mixed Electromagnetic Coupling Scheme," *Micromachines (Basel).*, vol. 15, no. 12, Dec. 2024, doi: 10.3390/MI15121426,.

[35] Y. Zhang, J. Xu, and A. Zhang, "Generative Model for Dual-Band Filters Based on Modified Complementary Split-Ring Resonators," *Electronics 2024, Vol. 13, Page 2321*, vol. 13, no. 12, p. 2321, Jun. 2024, doi: 10.3390/ELECTRONICS13122321.

[36] G. Revathi and S. Robinson, "Design and Implementation of Highly Selective and Compact Low Profile Bandpass Filter for 5G Mid-Band Frequency Applications," *Wirel. Pers. Commun.*, vol. 130, no. 1, pp. 363–375, May 2023, doi: 10.1007/S11277-023-10289-4/METRICS.

[37] B. Mohammadi, A. Valizade, J. Nourinia, and P. Rezaei, "Design of a compact dual-band-notch ultra-wideband bandpass filter based on wave cancellation method," *IET Microwaves, Antennas and Propagation*, vol. 9, no. 1, pp. 1–9, Jan. 2015, doi: 10.1049/IET-MAP.2014.0372;REQUESTEDJOURNAL:JOURNAL:17518733;WEBSITE:WEBSITE:IETRESEARCH;WGROUP:STRING:PUBLICATION.

[38] H. Nimehvari Varcheh, P. Rezaei, and S. Kiani, "A modified Jerusalem microstrip filter and its complementary for low phase noise X-band oscillator," *Int. J. Microw. Wirel. Technol.*, vol. 15, no. 10, pp. 1707–1716, Dec. 2023, doi: 10.1017/S1759078723000703.

[39] M. El Amine Chaib, M. Abri, H. Badaoui, and N. Cherif, "Bandpass Filters Based on Hybrid Structure of Substrate Integrated Waveguide (SIW) and Hilbert Defected Ground Structure (HDGS)," *Progress in Electromagnetics Research Letters*, vol. 104, pp. 27–35, 2022, doi: 10.2528/PIERL22032503.

Biography

Gauravkumar Asari is currently Assistant Professor at Department of Electronics and Communication Engineering, Vishwakarma Government Engineering College, Chandkheda-382424, Ahmedabad, Gujarat, India. He received his Bachelor's Degree in Electronics and Communication Engineering from Nirma Institute of Technology (Affiliated to Gujarat University), Ahmedabad, Gujarat, India in 2006, Master's Degree in Communication Systems from L.D. College of Engineering (Affiliated to Gujarat University), Ahmedabad, Gujarat, India, and PhD in Electronics and Communication Engineering from Gujarat Technological University, Ahmedabad, Gujarat, India in 2025. His current research interest are passive microwave devices, metamaterials and 5G communication systems.